Nuclear "pasta" structures in low-density nuclear matter and properties of the neutron-star crust

Minoru Okamoto,[1,2] Toshiki Maruyama,[2] Kazuhiro Yabana,[1,3] and Toshitaka Tatsumi[4]
[1]*Graduate School of Pure and Applied Science, University of Tsukuba, Tennoudai 1-1-1, Tsukuba, Ibaraki 305-8571, Japan*
[2]*Advanced Science Research Center, Japan Atomic Energy Agency, Shirakata Shirane 2-4, Tokai, Ibaraki 319-1195, Japan*
[3]*Center of Computational Sciences, University of Tsukuba, Tennoudai 1-1-1, Tsukuba, Ibaraki 305-8571, Japan*
[4]*Department of Physics, Kyoto University, Kyoto 606-8502, Japan*
(Received 10 April 2013; revised manuscript received 9 July 2013; published 5 August 2013)

In the neutron-star crust, nonuniform structure of nuclear matter—called the "pasta" structure—is expected. From recent studies of giant flares in magnetars, these structures might be related to some observables and physical quantities of the neutron-star crust. To investigate the above quantities, we numerically explore the pasta structure with a fully three-dimensional geometry and study the properties of low-density nuclear matter, based on the relativistic mean-field model and the Thomas-Fermi approximation. We observe typical pasta structures for fixed proton number fraction and two of them for cold catalyzed matter. We also discuss the crystalline configuration of "pasta."

DOI: 10.1103/PhysRevC.88.025801 PACS number(s): 21.65.−f, 26.60.Gj

I. INTRODUCTION

A neutron star has a radius of about 10 km and a mass of about 1.4 times the solar mass. It is considered to consist of four parts [1,2]. The region around 0.3 km from the surface is called the "outer crust," where Fe nuclei are expected to form a Coulomb lattice. The region around 0.3–1 km is called the "inner crust" with a density of about $0.3–0.5\rho_0$. There are neutron-rich nuclei in the lattice and dripped neutrons in a superfluid state. Two central regions with higher densities are called the "outer core" and the "inner core," in which proton superconductivity, neutron superfluidity [3], meson condensations [4–7], hyperon mixtures [8–11], or quark matter [12,13] are speculated to exist. The transition of matter composition with a change of density inside a neutron stars raises a question: Does it change smoothly or suddenly? A sudden change of matter property is generally accompanied by a first-order phase transition, which leads to the appearance of a mixed phase. Ravenhall *et al.* [14] suggested the existence of nonuniform structures of nuclear matter, i.e., a structured mixed phase. They suggested five types of geometrical structures: droplets, rods, slabs, tubes, and bubbles.[1] Due to their geometrical shapes that depend on the density, they are often referred to as "nuclear pasta" (e.g., spaghetti, lasagna, etc.) [14,19]. Many studies have suggested the existence of these pasta structures in low-density nuclear matter, relevant to the crust region of neutron stars and the collapsing stage of supernovae. The existence of pasta structures in the crust of neutron stars may not influence the bulk property and structure of neutron stars so much. However, it should be important for the mechanism of glitch, the cooling process of neutron stars, and the thermal and mechanical properties of supernova matter [20].

Recently, in the x-ray afterglow of giant flares quasiperiodic oscillations (QPOs) have been observed in some soft-γ-ray repeaters [21,22]. These flares are energetic γ-ray bursts from strongly magnetized neutron stars: magnetars. As one comprehensible understanding of the QPOs they may be attributed to the shear oscillations of neutron-star crust. Based on this interpretation, detailed information on neutron-star crust can be extracted from the QPOs [23], where the frequencies of shear oscillations depend on shear moduli of the Coulomb lattice of nuclei. Ogata *et al.* have calculated shear moduli using molecular dynamics simulations [24]. However, in this calculation, some important effects are missing; these include charge screening, finite-size effects of nuclei, and superfluidity of dripped neutrons [25]. In realistic situations, these elements should be taken into account in the elaborate calculation of shear moduli. Pasta structures should also be considered. Thus the energy change against a small deformation of the lattice can be discussed using shear moduli. On the other hand, if the energy change against a large deformation is known, the breaking strain of neutron-star crust can be obtained. Then, this breaking strain could determine the possible size of mountains on the neutron-star crust, which may radiate gravitational waves strongly under rapid rotation [26]. These waves may be detected by large-scale interferometers and could limit the spin frequencies of accreting stars. Furthermore, the breaking strain may be important for the "star quake" model of giant flares in magnetars [27].

The species and the sizes of the pasta structure are determined for given average baryon-number densities by minimizing the total energy density, which consists of the bulk, the surface, and the Coulomb energy densities. From the thermodynamical point of view, nuclear matter at subsaturation density can be represented by a dilute gas phase and a dense liquid phase in chemical equilibrium which determines particle densities in both phases. Once the averaged density is given, the volume fraction of gas or liquid phase is determined. Since the shape and size of the structure are independent of the bulk energy density due to the nuclear saturation property, they are

[1]Note that the emergence of an inhomogeneous structure is a general feature accompanying a noncongruent first-order phase transition [15,16], and there have been other known examples including hadron-quark deconfinement or meson condensation [17,18].

determined by the balance between the Coulomb and surface energy densities [28].

In many studies of nuclear pasta, the geometrical symmetry of the structure has been assumed by employing the Wigner-Seitz (WS) approximation [14,19]. In this approximation, one can find all the physical quantities from those in a single WS cell. Furthermore, the calculation is reduced to a one-dimensional form owing to the geometrical symmetry, which drastically saves the computational cost. On the other hand, by virtue of the recent development in computational science, it becomes possible to calculate without any assumption about the geometry of nonuniform structures [29,30]. In these studies, one imposes a periodic boundary condition in a small cubic cell, which includes only one period of structures. Although these studies yielded essentially the same results, i.e. typical pasta structures, it is hard to extract further information such as crystalline configuration of "pasta" and mechanical properties.

For detailed studies of the properties of the neutron-star crust, it is desired to perform three-dimensional calculations in a periodic cubic cell with sufficiently large sizes. Accordingly, we have developed a numerical code to calculate the density distribution of particles in a three-dimensional coordinate space and the relevant physical quantities, e.g., energy density or pressure of matter, by using a relativistic mean-field (RMF) model under the Thomas-Fermi approximation [31]. We have explored ground states of low-density nuclear matter with a fixed proton number fraction Y_p and observed a series of typical pasta structures appearing as the ground states. We have also observed crystalline configurations of droplets, rods, tubes, and bubbles. One of our findings is the appearance of a face-centered cubic (fcc) lattice of droplets in the ground state. However, the system was limited to the cases with fixed proton number fraction and detailed discussion is still needed about its appearance.

In this article, first we explore the pasta structures and properties of low-density charge-neutral nuclear matter with a fixed proton number fraction, following the line of our previous study in Ref. [31] but in more detail: We present more refined results obtained by using a fine grid width of 0.3 fm, instead of 0.8 fm. We also extend the region of the data points into the lower density region. Second, as a new research target, we explore catalyzed matter relevant to the neutron-star crust, where a significant difference between results with and without the WS approximation can be seen. It is possible to extend our framework to finite temperatures as in the case of proto-neutron star matter [32,33], but, in this article, we concentrate on the cold neutron-star crust for simplicity.

In Sec. II, we present the model and describe our numerical procedure. In Sec. III, we first demonstrate some results from our three-dimensional calculation for low-density nuclear matter with fixed proton number fraction $Y_p = 0.5$, 0.3, and 0.1 that may be related to supernova matter and newly born hot proto-neutron star crust. Then, in the second part of Sec. III, we investigate the pasta structures at β equilibrium, as they occur in cold neutron stars, and the crystalline configuration of nuclear pasta. Finally, Sec. IV is devoted to a summary and concluding remarks.

II. MODEL AND METHOD

Several many-body techniques have been used for studying the pasta structures in the literature, including the compressible liquid-drop model (CLDM) [14,19,34–36], the Thomas-Fermi model [29,33,37–39], the Hartree-Fock (HF) approximation employing effective NN interactions [30,40,41], and quantum molecular dynamics (QMD) [42–44]. In the studies using the CLDM and the Thomas-Fermi model, the WS approximation was always used and only typical pasta structures were used. In QMD calculations, one does not assume any specific nonuniform structure of nuclear matter, though a uniform background of electrons is assumed. Some of the Thomas-Fermi calculations and the HF calculations used a periodic boundary condition but no geometrical symmetry was assumed for the structure. However, the size of the periodic unit cell was not large enough for quantitative discussion. In this paper, to describe the interaction among nucleons, we employ an RMF model under the Thomas-Fermi approximation [39]. The model treats the mean fields of sigma, omega, and rho mesons represented by σ, ω^μ, and $\mathbf{R}^\mu$, respectively, together with nucleons ψ, electrons ψ_e, and the electromagnetic field A_μ, by a Lagrangian $\mathcal{L}$ introduced in a Lorentz-invariant form as follows:

$$\begin{aligned}\mathcal{L} = \bar{\psi}\Big[& i\gamma^\mu\partial_\mu - m_N^* - g_{\omega N}\gamma^\mu\omega_\mu - g_{\rho N}\gamma^\mu\boldsymbol{\tau}\cdot\boldsymbol{R}_\mu \\ & - e\frac{1+\tau_3}{2}\gamma^\mu A_\mu\Big]\psi + \frac{1}{2}(\partial_\mu\sigma)^2 - \frac{1}{2}m_\sigma^2\sigma^2 - U(\sigma) \\ & - \frac{1}{4}\omega_{\mu\nu}\omega^{\mu\nu} + \frac{1}{2}m_\omega^2\omega_\mu\omega^\mu - \frac{1}{4}\boldsymbol{R}_{\mu\nu}\boldsymbol{R}^{\mu\nu} + \frac{1}{2}m_\rho^2\boldsymbol{R}_\mu\boldsymbol{R}^\mu \\ & - \frac{1}{4}F_{\mu\nu}F^{\mu\nu} + \bar{\psi}_e[i\gamma^\mu\partial_\mu - m_e + e\gamma^\mu A_\mu]\psi_e, \end{aligned} \tag{1}$$

where $U(\sigma) = \frac{1}{3}bm_N(g_{\sigma N}\sigma)^3 - \frac{1}{4}c(g_{\sigma N}\sigma)^4$ is a nonlinear term for the scalar field, $m_N^* = m_N - g_{\sigma N}\sigma$ represents the effective mass of the nucleon, $\omega_{\mu\nu} = \partial_\mu\omega_\nu - \partial_\nu\omega_\mu$, $\boldsymbol{R}_{\mu\nu} = \partial_\mu\boldsymbol{R}_\nu - \partial_\nu\boldsymbol{R}_\mu - g_{\rho N}(\boldsymbol{R}_\mu\times\boldsymbol{R}_\nu)$, $F_{\mu\nu} = \partial_\mu A_\nu - \partial_\nu A_\mu$, and g_{ab} represent the coupling constant between a and b. The thermodynamic potential Ω is then given by $\Omega = E - \sum_{i=n,p,e}\mu_i\int d^3r\rho_i(\mathbf{r})$ in terms of the total energy E, number densities $\rho_i(\mathbf{r})$ and chemical potentials μ_i. Variation of Ω with respect to each field gives the field equation.

The set of coupled field equations for the mean fields and the Coulomb potential $A^\mu = (V_{\rm Coul}, \mathbf{0})$ renders

$$-\nabla^2\sigma(\mathbf{r}) + m_\sigma^2\sigma(\mathbf{r}) = g_{\sigma N}\big[\rho_p^s(\mathbf{r}) + \rho_n^s(\mathbf{r})\big] - \frac{dU}{d\sigma}, \tag{2}$$

$$-\nabla^2\omega_0(\mathbf{r}) + m_\omega^2\omega_0(\mathbf{r}) = g_{\omega N}[\rho_p(\mathbf{r}) + \rho_n(\mathbf{r})], \tag{3}$$

$$-\nabla^2 R_0(\mathbf{r}) + m_\rho^2 R_0(\mathbf{r}) = g_{\rho N}[\rho_p(\mathbf{r}) - \rho_n(\mathbf{r})], \tag{4}$$

$$\nabla^2 V_{\rm Coul}(\mathbf{r}) = 4\pi e^2[\rho_p(\mathbf{r}) - \rho_e(\mathbf{r})], \tag{5}$$

where $\rho_i^s(\mathbf{r}) = \langle\bar{\psi}_i(\mathbf{r})\psi_i(\mathbf{r})\rangle$, $i = p, n$, is the nucleon scalar density and R_0 is the third component of the isovector field $\mathbf{R}_\mu$. Field equations for fermions simply yield the standard relations between the densities ρ_i and chemical potentials μ_i

TABLE I. Parameter set used in the RMF model.

$g_{\sigma N}$	$g_{\omega N}$	$g_{\rho N}$	b	c	m_σ (MeV)	m_ω (MeV)	m_ρ (MeV)
6.3935	8.7207	4.2696	0.008659	−0.002421	400	783	769

within the Thomas-Fermi approximation,

$$\mu_n = \sqrt{k_{\mathrm{F},n}(\mathbf{r})^2 + m_N^*(\mathbf{r})^2} + g_{\omega N}\omega_0(\mathbf{r}) - g_{\rho N} R_0(\mathbf{r}), \quad (6)$$

$$\mu_p = \sqrt{k_{\mathrm{F},p}(\mathbf{r})^2 + m_N^*(\mathbf{r})^2} + g_{\omega N}\omega_0(\mathbf{r}) + g_{\rho N} R_0(\mathbf{r}) - V_{\mathrm{Coul}}(\mathbf{r}), \quad (7)$$

$$\rho_e(\mathbf{r}) = (\mu_e - V_{\mathrm{Coul}}(\mathbf{r}))^3/3\pi^2, \quad (8)$$

where the local Fermi momentum $k_{F,i}(\mathbf{r})$ is simply related to the density, $k_{F,i}^3(\mathbf{r})/(3\pi^2) = \rho_i(\mathbf{r})$. Finally, baryon-number conservation and charge neutrality are imposed besides these equations. We use the same set of parameters as in Ref. [39] listed in Table I, in order to compare the equation of state (EOS) and structural changes of the pasta structure with and without the WS approximation. With these parameters, we can reproduce the properties of uniform nuclear matter shown in Table II. The first and second quantities, ρ_0 and ϵ_0, are the saturation density of symmetric nuclear matter (≈ 0.16 fm^{-3}) and its energy per nucleon, respectively. The third and forth quantities, K and S_0, are the incompressibility and symmetry energy at ρ_0, respectively. The last one, L, is the slope parameter of symmetry energy at ρ_0. By using these parameters the binding energy per nucleon around the saturation density is expressed as

$$\frac{E}{A} = \epsilon_0 + \frac{K(\rho-\rho_0)^2}{18\rho_0^2} + \left[S_0 + \frac{L(\rho-\rho_0)}{3\rho_0}\right](1-2Y_p)^2. \quad (9)$$

To numerically simulate the nonuniform structure of infinite matter, we use a cubic cell with a periodic boundary condition. If the cell size is small and includes only one or two units of the structure, the geometrical shape should be affected by the boundary condition and the appearance of some structures is implicitly suppressed. Therefore, the cell size should be so large as to include several units of the pasta structure. We divide the cell into three-dimensional grids. The desirable grid width should be so small as to describe the detailed density distribution, particularly at the nuclear surface. Due to this requirement, we set the grid width to 0.3 fm at the largest. This grid width is small enough to give an energy difference within 2 keV from that with 0.1 fm. Given the average baryon-number density ρ_B, the initial density distributions of fermions are randomly prepared on each grid point. Then proper density distributions and the meson mean fields are searched for until the chemical potentials are independent of the position.

TABLE II. EOS of uniform nuclear matter.

ρ_0 (fm^{-3})	ϵ_0 (MeV)	K (MeV)	S_0 (MeV)	L (MeV)
0.153	−16.4	240	33.4	84

More detailed numerical procedures and treatment with a local chemical potential will be discussed in the Appendix.

III. RESULTS

A. Fixed proton number fraction

First, we present here some results for fixed proton number fraction Y_p with $Y_p = 0.5$ (symmetric nuclear matter), 0.3, and 0.1, which are roughly relevant to supernovae and neutron-star crust. Shown in Fig. 1 are the proton density distributions in cold symmetric matter. We can see that the typical pasta phases with rods, slabs, tubes, and bubbles, in addition to spherical nuclei (droplets), are reproduced by our calculation in which no assumption on the structures was used. Furthermore, these cells include several units and we can specify these lattice structures. The crystalline configuration of droplets and bubbles is fcc; rods and tubes exhibit a honeycomb configuration.

No exotic mixtures appear as ground states at any density. In a droplet, we have seen that the proton density is highest near the surface due to Coulomb repulsion, while the neutron density distribution is flat inside the droplet. Note that baryon density outside the droplets is zero for $Y_p = 0.3$ and 0.5. Electron density is spread over all space but slightly localized

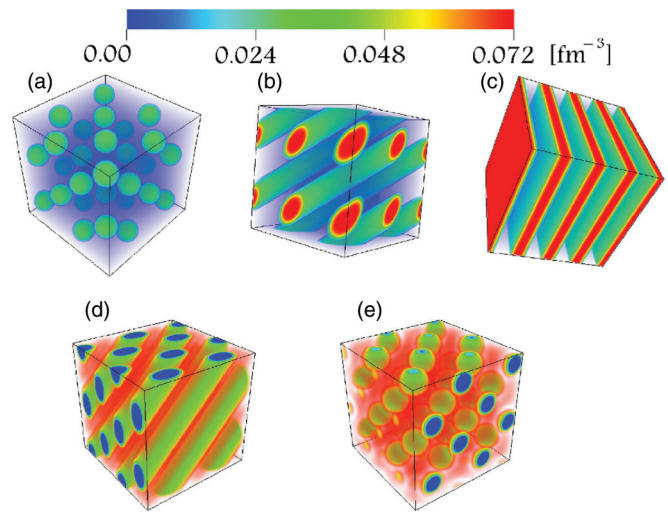

FIG. 1. (Color online) Proton density distributions in the ground states of symmetric matter ($Y_p = 0.5$). Typical pasta phases are observed: (a) Spherical droplets with an fcc crystalline configuration at baryon density $\rho_B = 0.01$ fm^{-3}, of 98 fm each side. (b) Cylindrical rods with a honeycomb crystalline configuration at 0.024 fm^{-3}, of 76 fm each side. (c) Slabs at 0.05 fm^{-3}, of 95 fm each side. (d) Cylindrical tubes with a honeycomb crystalline configuration at 0.08 fm^{-3}, of 79 fm each side. (e) Spherical bubbles with an fcc crystalline configuration at 0.09 fm^{-3}, of 97 fm each side.

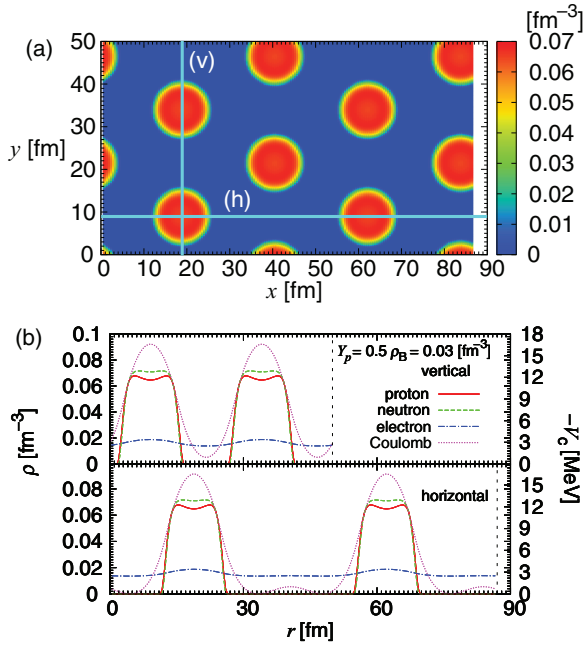

FIG. 2. (Color online) (a) Proton density distribution in the rod phase ($\rho_B = 0.03$ fm^{-3} for $Y_p = 0.5$) on the sliced plane. (b) The density distribution along a line (v) (vertical) and (h) (horizontal) in the upper figure. Red (solid) lines indicate protons, green (dashed) lines neutrons, blue (dot-dashed) lines electrons, and pink (dotted) lines the Coulomb potential.

around the droplets, which brings about the charge-screening effect.

We can see the density distribution of fermions for $Y_p = 0.5$ and $\rho_B = 0.03$ fm^{-3} in Fig. 2 and find the unique features of the three-dimensional calculation. Here, in the upper panel, we show the proton density distribution on a sliced plane and depict the two kinds of density profiles of protons, neutrons, and electrons and the Coulomb potential in the lower panel. One is along a vertical line (v) which passes through the rods; another is along a horizontal one (h). From this figure, the advantage of the three-dimensional calculation can be seen. The proton, neutron, and electron density distributions are almost the same for both the cases of (v) and (h). However, a slight difference appears in the Coulomb potential. We have set the maximum value of the Coulomb potential to be zero for convenience. In the case of the rod phase, that point corresponds to the centroid of the triangular lattice. These points are included not on the path (v) but on the path (h). Considering the importance of the distinct relation between the Coulomb and surface energies for the pasta structure, we should take into account this anisotropy in a proper way.

In Fig. 3 we show the energy, total pressure, and baryon partial pressure as functions of density. Baryon partial pressure is given by subtracting the electron contribution from the total pressure. Note that the energy $E/A - m_N$ includes the kinetic energy of electrons, which makes the total pressure positive. This density dependence is qualitatively the same as the one with the WS approximation. The appearance of nonuniform structures will make nuclear matter more stable: the energy per baryon gets lower up to about 15 MeV/A compared to uniform matter and the pressure per baryon gets higher up to about 0.5 MeV/A.

We have obtained almost the same EOS as that given by the WS approximation, in which the same RMF model is applied. However, one of the differences between our results and those with the WS approximation appears in the existence region of each pasta structure; the density region of the rod is wider and the tube narrower in our calculation. Since the energy differences between different structures are quite small, the crystalline configuration might affect the appearance of each pasta structure.

We get the same result for the crystalline structure of droplets as discussed in Ref. [31]. In the medium-density region, an fcc lattice is more favored than a body-centered cubic (bcc) lattice. In the QMD calculations [43] that precede the present calculation without geometrical structures being assumed, droplets form a bcc lattice. This difference might come from the treatment of electrons or the charge-screening effect since a uniform electron distribution has been assumed in the QMD calculation. To see the effects of the electron distribution on the crystalline configuration, let us compare two cases within our framework: one is the full calculation and the other is the case for which uniformly distributed electrons are assumed. In the latter calculation, the Coulomb potential $V_{\rm Coul}$ in Eq. (8) is replaced by a constant $V_0 = 0$ and $\rho_e = (\mu_e - V_0)^3/3\pi^2$. However, in the case of uniformly distributed electrons, gauge invariance is partially violated, since we replace $V_{\rm Coul}$ by V_0 in the equation for the electron chemical potential but retain $V_{\rm Coul}$ in the equation for the proton chemical potential and thus in the expression for the proton number density. In this case, the droplets have a smaller size compared with that in the full calculation in throughout the density region of the droplet phase. This means that the Coulomb repulsion among protons is slightly weaker in the full calculation due to the screening by electrons. One can see this difference in Table III. Here, R_d and $R_{\rm latt}$ are defined as follows:

$$\frac{V}{N_d} = \frac{4\pi}{3} R_{\rm latt}^3, \tag{10}$$

$$R_d = R_{\rm latt} \left(\frac{\langle \rho_p \rangle^2}{\langle \rho_p^2 \rangle} \right)^{1/3}, \tag{11}$$

where V denotes the cell volume, N_d the number of droplets in the cell, and the brackets $\langle \ldots \rangle$ mean the average over the cell volume. In our previous study using the WS approximation [39], a similar discussion was presented. We argued that the charge-screening effect is not so remarkable due to the large Debye screening length. Indeed, the crystalline configuration does not change in our present calculation. Thus, it is confirmed that charge screening by electrons does not affect the crystalline configuration significantly. This difference in crystalline configuration between the QMD calculation and the present calculation remains to be elucidated as a future problem.

We obtain the typical pasta structure as a ground state for any proton number fraction above 0.1. Also in the cases of $Y_p = 0.3$ and 0.1, the fcc lattice of droplets is energetically more favorable than the bcc one. In Fig. 4 we depict the density

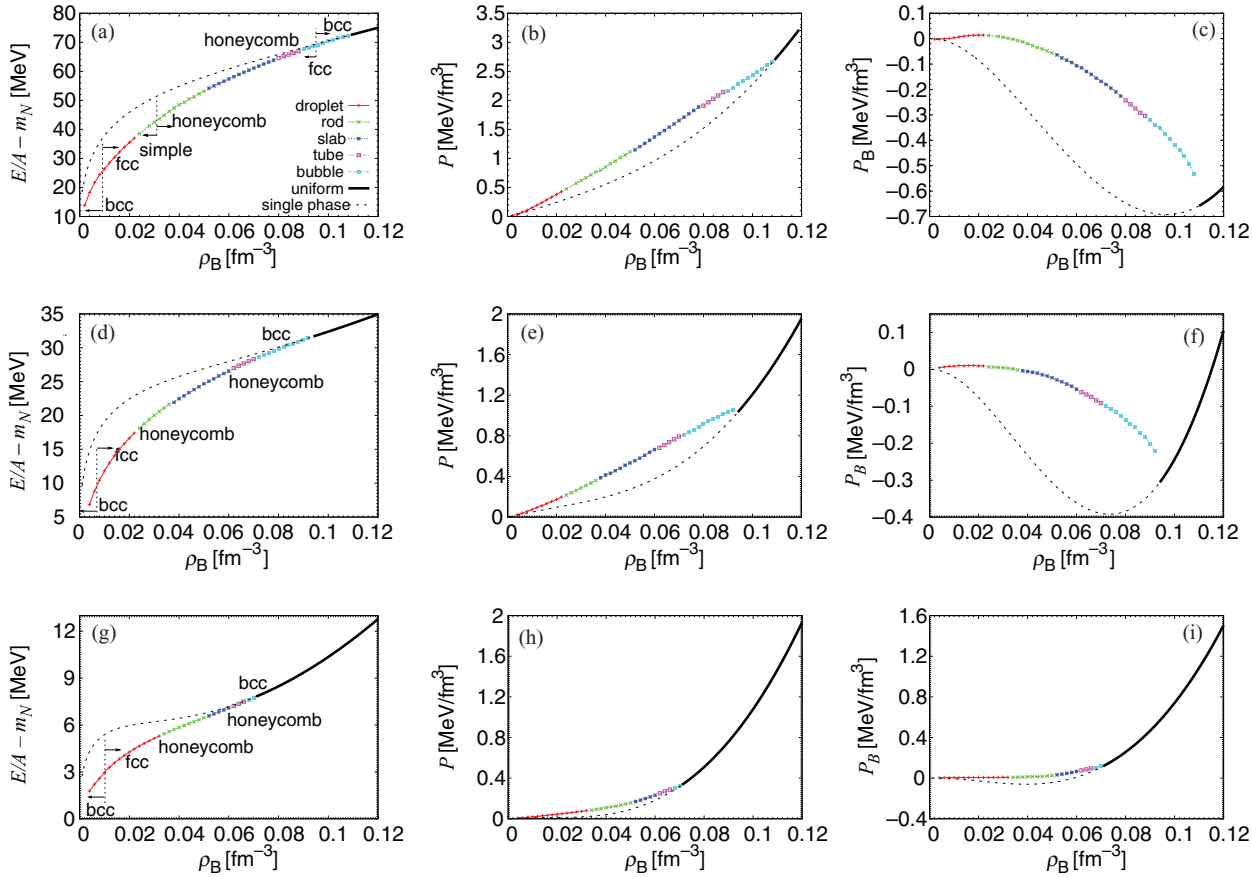

FIG. 3. (Color online) From the left, energy [(a), (d), and (g)], pressure [(b), (e), and (h)], and baryon partial pressure [(c), (f), and (i)] of $Y_p = 0.5$ [(a), (b), and (c)], 0.3 [(d), (e), and (f)], and 0.1 [(g), (h), and (i)] in this order from the upper panel. Red lines (with pluses) indicate droplets, green (with crosses) rods, blue (with stars) slabs, magenta (with open squares) tubes, cyan (with full squares) bubbles, and black uniform, respectively. The transition density from bcc droplet to fcc droplet exists around 0.010 fm^{-3} for $Y_p = 0.5$, 0.007 fm^{-3} for $Y_p = 0.3$, and 0.010 fm^{-3} for $Y_p = 0.1$, respectively. All the transition densities among different crystalline configurations, including the ones indicated in the figure, have numerical ambiguity of 0.002 fm^{-3}.

profiles of protons, neutrons, electrons and the Coulomb potential for $Y_p = 0.3$ and 0.1 with baryon number density 0.03 fm^{-3} along a line which passes through the rods in the same way as in Fig. 2. While for $Y_p = 0.3$ there appear vacant regions of neutrons, the neutron density is finite at any point for $Y_p = 0.1$: the space is filled with dripped neutrons. Even in the case of $Y_p = 0.1$, we can see that the proton density is highest around the surface due to Coulomb repulsion.

B. Catalyzed matter

Cold catalyzed matter requires β equilibrium instead of the fixed proton number fraction: $\mu_n = \mu_p + \mu_e$. Shown in Fig. 5 are the proton density distributions in the ground states for cold catalyzed nuclear matter. We have obtained the bcc lattice of droplets, fcc lattice of droplets, and honeycomb lattice of rods, depending on density. In Fig. 6, the density profiles of fermions in the bcc and fcc lattices of droplets and the Coulomb potential are depicted along a line which passes through the droplets for $\rho_B \approx 0.01$ fm^{-3} and $\rho_B \approx 0.03$ fm^{-3}. The effect of Coulomb repulsion can be seen where the proton density is highest near the surface, while the neutron density distribution is flat inside the droplet. We have observed only those three structures (a), (b), and (c) in Fig. 5. This result is consistent with the previous study of the relation between the density region of the pasta structure and the slope parameter L in Eq. (10) [45]. The larger the value of L is given, the narrower

TABLE III. The radii of droplets obtained from the full calculation and with uniformly distributed electrons.

ρ_B (fm^{-3})	0.004	0.01	0.016	0.022
R_d (full calculation) (fm)	6.09	6.67	7.23	7.79
R_d (uniform electron distribution) (fm)	5.91	6.40	7.01	7.64

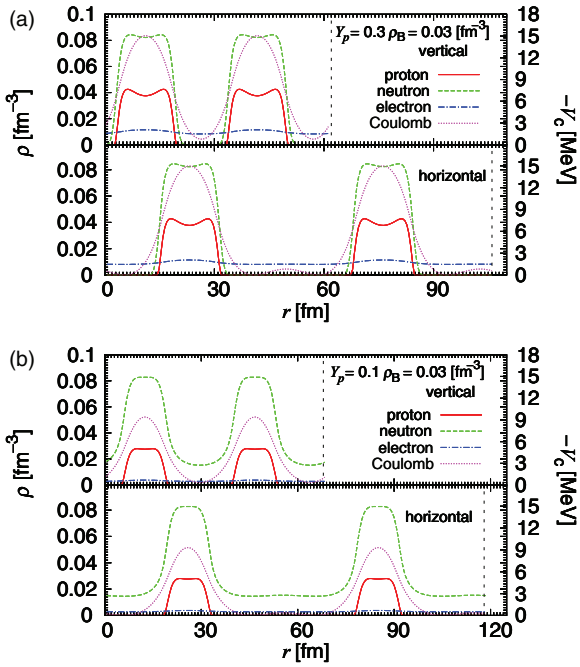

FIG. 4. (Color online) Density distributions of protons, neutrons, and electrons and the Coulomb potential of rods in $\rho_B = 0.03$ fm^{-3} [(a) $Y_p = 0.3$; (b) $Y_p = 0.1$]. Red (solid) lines indicate protons, green (dashed) lines neutrons, blue (dot-dashed) lines electrons, and pink (dotted) lines the Coulomb potential.

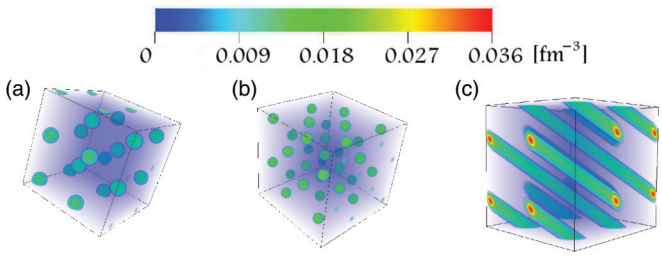

FIG. 5. (Color online) Proton density distributions for (a) droplets (bcc) at $\rho_B = 0.01$ fm^{-3}, of 194 fm each side, (b) droplets (fcc) at $\rho_B = 0.03$ fm^{-3}, of 162 fm each side, and (c) rods (honeycomb) at $\rho_B = 0.056$ fm^{-3}, of 144 fm each side.

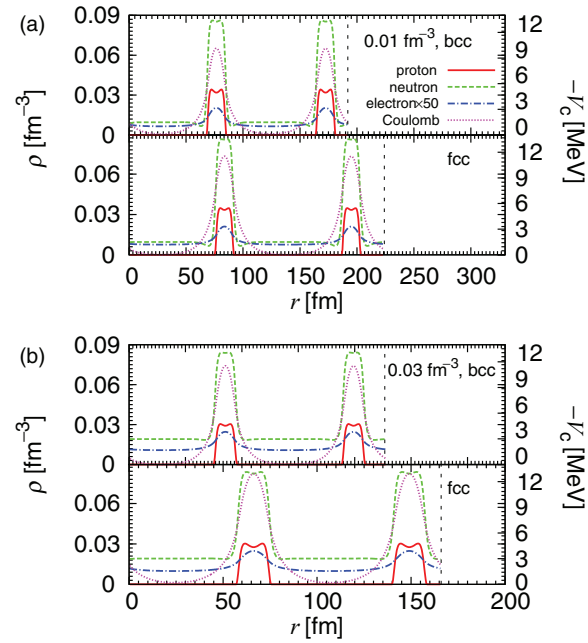

FIG. 6. (Color online) Density distributions of protons, neutrons, and electrons and the Coulomb potential in the fcc and bcc lattices [(a) $\rho_B = 0.01$ fm^{-3}; (b) $\rho_B = 0.03$ fm^{-3}]. In each panel (a) and (b), the upper figure shows the case of bcc and the lower the case of fcc. Red (solid) lines indicate the proton, green (dashed) lines neutron, and blue (dot-dashed) lines electron (multiplied by a factor of 50) density distributions; the pink (dotted) lines show the Coulomb potential and black dashed lines are the lattice constant.

the pasta region is. In our calculation, L is about 80 MeV, which is close to the critical value ≈90 MeV in the CLDM, where the pasta structures do not appear. In the previous calculation using the WS approximation, only the droplet structure appeared as a ground state [39]. However, in our three-dimensional calculation using the same RMF framework, the rod structure also appears.

We show the density dependence of the total energy, the Coulomb energy, and the proton number fraction in Fig. 7. To see the difference between droplets in the bcc and fcc lattices, we plot the density dependence of the size of the droplet, the lattice constant, the volume fraction, the proton number in each droplet, and the proton number fraction in Fig. 8. Here, the meanings of R_d and $R_{\rm latt}$ are the same as in Eqs. (10) and (11).

The density dependence of the ground-state energy is shown in the left panel of Fig. 7. We can see that the ground-state configuration changes depending on density. In the lower density region, droplets with the bcc lattice appear. Around $\rho_B \approx 0.01$ fm^{-3}, the lattice structure changes from bcc to fcc. A remarkable change occurs around $\rho_B \approx 0.052$ fm^{-3}: from the fcc lattice of droplets to the honeycomb lattice of rods. It is hard to see the total energy difference between the bcc and fcc lattices of droplets. That of the proton number fraction at $\rho_B < 0.01$ fm^{-3} is also hard to distinguish in the right panel of Fig. 7. However, there are significant differences in the proton number fraction at $\rho_B > 0.01$ fm^{-3} and the Coulomb energy, as shown in the middle panel of Fig. 7.

As in the case of fixed proton number fraction, there emerges an fcc lattice of droplets near the transition density from the droplet phase to another in our calculation, while it has been regarded in the previous studies that a bcc lattice appear [34]. Almost the same radii and density distributions of droplets, proton number fraction, and proton number in nuclei are obtained for both crystalline configurations (see the right panel of Fig. 8 at $\rho_B < 0.01$ fm^{-3}). The difference between the bcc and fcc lattices may be seen only in the Coulomb energy: the Coulomb energy of the fcc lattice is a little higher than that of the bcc lattice. However, near the transition density from droplet to rod, the radius of droplets and the proton number fraction are different between the bcc and fcc lattices even if their baryon-number densities are the same (see Fig. 8 at $\rho_B \approx 0.02$ fm^{-3}):

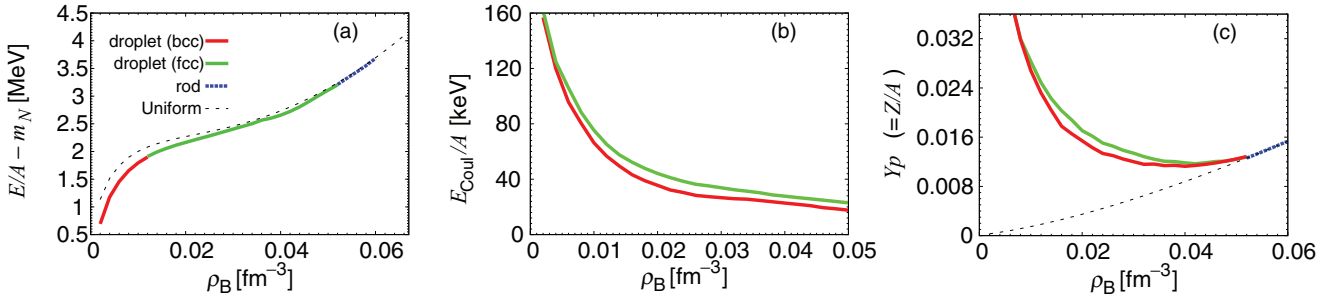

FIG. 7. (Color online) From the left, the total energy, the Coulomb energy, and the proton number fraction. Red (black) lines indicate fcc droplets, green (gray) lines bcc droplets, and blue (short dashed) lines rods, respectively. Dotted lines are for the case of a single phase.

the size of the droplet and the proton number fraction in the fcc lattice are 7.54 fm and 0.016, respectively, while those in the bcc lattice are 7.01 fm and 0.014. Because the size of droplets and the proton number fraction are different, the Coulomb energy alone is no longer the criterion of the ground state. We should also take into account the size of droplets and the proton number fraction in order to obtain the ground state. Roughly speaking, the larger the radius of droplets is, the smaller the surface energy is. While the Coulomb energy of the fcc lattice is larger than that of the bcc lattice in all the regions of the droplet phase, the total energy of the fcc lattice is less than that of the bcc lattice by the gain of surface energy.

Because we cannot take into account shell effects [46], the proton number continuously decreases with increase of baryon number density. To compare the density dependence of the proton number within the same interaction for baryons, our model might be similar to type B in Ref. [45]. In our model, the slope parameter of symmetry energy L is a little larger than that in Ref. [45], so that the proton number converges to about 35 in the low-density limit, while it converges to about 40 in Ref. [45]. This result is consistent with the relationship between L and the proton number in the droplet.

The maximum size of the droplet can be estimated by the Bohr-Wheeler condition as $E^{(0)}_{\rm Coul} > 2E_{\rm surf}$ [47]. The "virial" theorem for the pasta structure reads $E_{\rm surf} = 2E_{\rm Coul}$, where $E^{(0)}_{\rm Coul}$ is the Coulomb energy of an isolated nucleus and the Coulomb energy of a nucleus in matter is $E_{\rm Coul} \approx E^{(0)}_{\rm Coul}(1 - 3u^{1/3}/2)$. From these equations, the appearance of nonspherical nuclei in nuclear matter has been expected for a volume fraction $u > 0.125$. However, in our calculation,

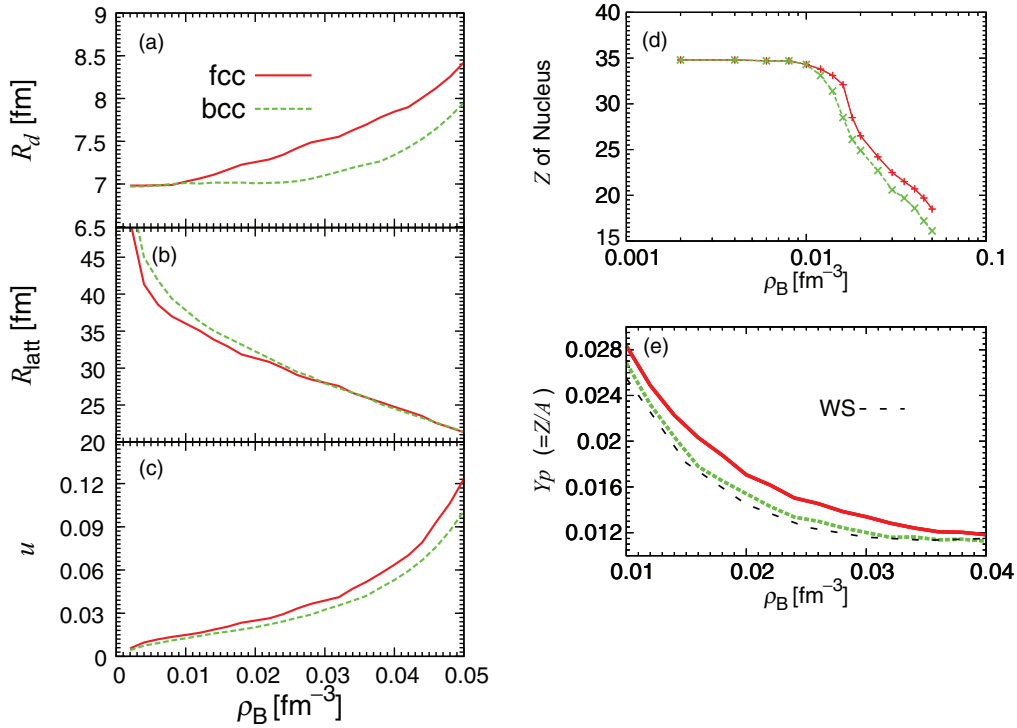

FIG. 8. (Color online) (a) The density dependence of radii of nuclei, (b) lattice constants, and (c) the volume fraction. The proton number of nuclei and the proton number fraction are in panels (d) and (e), respectively. The red (solid) lines in each panel indicate fcc and the green (dashed) lines indicate bcc in comparison with results from the WS approximation.

the structural change from droplet to rod occurs around $u \approx 0.1$ (see the value at $\rho_B \approx 0.05$ fm^{-3} in Fig. 8). This means that considering the nonuniformity of the electrons is worthwhile for "pasta" structures, because the relation between the Coulomb energy of a cell and that of a nucleus has been derived by using a uniform background of electrons and uniform baryon density inside a nucleus. The effect of the screening by charged particles, which is properly included in our calculation, may be one of the origins of this difference. To reach a final conclusion on this issue, we should perform another calculation with uniformly distributed electrons and confirm the effects of electron nonuniformity. Also the difference in the droplet surface may give another reason: the CLDM treated droplets with a sharp surface, while our droplets have a diffuse surface. The same discussion may apply to the QMD calculation for the case of fixed proton number fraction.

At low density, where the volume fraction of droplets is less than 1%, we can regard nuclei as point particles even if there is a broad distribution of neutrons. However, near the transition density from droplet to rod, the volume fraction amounts to about 10% and the distance between the nuclei is very small, which is one reason for the shape transition. In this region, the approximation for each droplet as a point particle is not valid.

IV. SUMMARY AND CONCLUDING REMARKS

We have numerically explored nonuniform structures and discussed the properties of low-density nuclear matter with charge neutrality and cold catalyzed matter, using the RMF model under the Thomas-Fermi approximation. Without any assumption about the geometric structure, we have carried out fully three-dimensional calculations in large cubic cells with a periodic boundary condition.

First, we explored low-density nuclear matter with fixed proton number fractions of $Y_p = 0.5$, 0.3, and 0.1, which may be relevant to supernova explosions and newly born proto-neutron stars. With an increase of density, which ranges from well below to around the normal nuclear density, we have observed the typical pasta structures as a ground state for each density and proton number fraction. The appearance of the pasta structures lowers the energy, while the energy differences between various geometrical structures are very small. We improved the EOS by adopting the precise grid width and exploring to lower density. In our previous study, we applied the grid width up to 0.8 fm. As mentioned before, large meshes affect the density regions of each pasta structure and the EOS. By calculating at about twice the resolution, we got almost the same results but a smoother EOS.

Second, we extended our calculations to cold catalyzed matter which corresponds to the neutron-star crust. In this case, with an increase of density, which ranges from well below to half of the normal nuclear density, we have observed that the ground state of matter shows two types of pasta structures: droplets and rods. For the crystalline configuration of droplets, near the transition density to rods, the fcc lattice is more favorable than the bcc lattice, which is different from the results of previous studies. We have discussed some reasons for the difference, but more elaborate studies are needed to clarify it.

We found that the ground state of low-density nuclear matter changes its crystalline configuration from a bcc to an fcc lattice near half the normal nuclear density within the RMF model. This conclusion arises from including the smooth surface of nuclei and a self-consistent calculation of the Coulomb interaction. There are, however, several other forms of lattice structures (e.g., hexagonal closest packing and tetrahedral). The hexagonal lattice has the same filling factor as the fcc one. There are many possibilities, but there is no specific interpretation for the crystalline configuration in the ground state.

In application to the neutron-star crust, it is interesting and might be important to investigate the shear modulus. Using the density distribution obtained by our three-dimensional calculation for cold catalyzed matter (droplets and rods), we can estimate the shear modulus, in which charge-screening and finite-size effects are properly taken into account. More interestingly, one may directly calculate the breaking strain by considering the large deformation of the lattice. These issues will be discussed in a separate paper.

For newly born neutron stars, as in supernova explosions, finite-temperature and neutrino-trapping effects become important, as do the dynamics of the first-order phase transition with formation of the structures. It would be also interesting to extend our framework to include these effects.

ACKNOWLEDGMENTS

We thank H. Sotani for his useful comments. This work is supported by the project "Research on the Emergence of Hierarchical Structure of Matter by Bridging Particle, Nuclear and Astrophysics in Computational Science," 2008–2013, of the Grant-In-Aid for Scientific Research on Innovative Areas, MEXT, Japan.

APPENDIX: CHEMICAL POTENTIAL

In general, particles tend to move from a higher chemical potential to a lower one. A simple example is a system of dilute molecules diffusing in a homogeneous environment. In this system, the molecules tend to move from areas with high concentration to low concentration, until the concentration is the same everywhere. Invoking this idea of chemical potential, we introduce a local chemical potential as a criterion of convergence to search the ground state.

In this Appendix, we first verify the relation between the ground state and uniform distribution of the local chemical potential. Then, the numerical procedures concerning the local chemical potential are explained.

We start by defining a local chemical potential as

$$\mu(r) = \frac{d\epsilon(r)}{d\rho(r)}, \tag{A1}$$

where $\rho(r)$ and $\epsilon(r)$ denote the density and energy density, respectively. Let us consider an exchange of material between two small-volume components ΔV at r_1 and r_2 conserving the

total amount of material as

$$\Delta\rho(r_1)\Delta V = -\Delta\rho(r_2)\Delta V \quad \text{(A2)}$$
$$\equiv \Delta\rho\Delta V. \quad \text{(A3)}$$

Then, the change of total energy is described as

$$\Delta E = [\Delta\epsilon(r_1) + \Delta\epsilon(r_2)]\Delta V \quad \text{(A4)}$$
$$= \left(\frac{d\epsilon(r_1)}{d\rho(r_1)}\Delta\rho(r_1) + \frac{d\epsilon(r_2)}{d\rho(r_2)}\Delta\rho(r_2)\right)\Delta V \quad \text{(A5)}$$
$$= [\mu(r_1)\Delta\rho(r_1) + \mu(r_2)\Delta\rho(r_2)]\Delta V \quad \text{(A6)}$$
$$= [\mu(r_1) - \mu(r_2)]\Delta\rho\Delta V. \quad \text{(A7)}$$

If the system is in its ground state, the energy should be stationary against any small density change $\Delta\rho$,

$$\frac{\Delta E}{\Delta\rho\Delta V} = 0, \quad \text{(A8)}$$

which reads

$$\mu(r_1) = \mu(r_2). \quad \text{(A9)}$$

From the above discussion, it is clear that uniform local chemical potential reflects that the system is in its ground state.

Next, we show the numerical procedure to get the ground state with the local chemical potential and avoid metastable states. Giving the average baryon-number density ρ_B, initial density distributions of fermions are randomly prepared on each grid point. Then proper density distributions and the meson mean fields are searched for. We introduce the local chemical potentials $\mu_a(\mathbf{r})$ $(a = p, n, e)$ to obtain the density distributions of baryons and electrons. The equilibrium state is eventually determined so that the chemical potentials are independent of the position. An exception is the region with no particle density, where the chemical potential of that particle can be higher [see Fig. 9(a) for more explanation]. Note that if the local density is zero, Eq. (A5) does not apply and there is no contradiction between this explanation and the present paragraph. We repeat the following procedures to attain

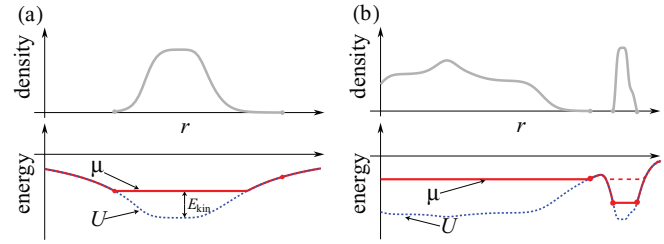

FIG. 9. (Color online) (a) Schematic figure of density distribution and the chemical potential with a constant mass subtracted. In the region with zero density, where the kinetic energy is zero, the chemical potential $\mu(\mathbf{r})$ is identical to the potential $U(\mathbf{r})$, while the chemical potential in the region with finite particle density is constant. (b) Schematic figure of nonuniform matter with an isolated matter region, where the chemical potential is different from that of the global one. By using the procedure to adjust densities between only the neighboring grids, such unphysical regions of isolated matter may appear.

uniformity of the chemical potentials. A chemical potential $\mu_i(\mathbf{r})$ of a baryon $i = p, n$ on a grid point $\mathbf{r}$ is compared with those on the six neighboring grids $\mathbf{r}' = \mathbf{r} + d\mathbf{r}$, $(d\mathbf{r} = \pm d\mathbf{x}, \pm d\mathbf{y}, \pm d\mathbf{z})$. If the chemical potential at the point under consideration is larger than that of another $\mu_i(\mathbf{r}) > \mu_i(\mathbf{r}')$, some part of the density will be transferred to the other grid point. This adjustment of the density distribution is simultaneously done on all the grid points. In addition to the above process, we adjust the particle densities between distant grid points chosen randomly in order to eliminate regions with different μ_i which can happen to isolated matter regions as in Fig. 9(b). The meson mean fields and the Coulomb potential are obtained by solving Eqs. (2)–(5) using the baryon density distributions $\rho_i(\mathbf{r})$ $(i = p, n)$ and the charge density distribution $\rho_p(\mathbf{r}) - \rho_e(\mathbf{r})$. The electron density $\rho_e(\mathbf{r})$ is directly calculated from the Coulomb potential $V_{\rm Coul}(\mathbf{r})$ and the electron chemical potential μ_e as $\rho_e(\mathbf{r}) = (\mu_e - V_{\rm Coul})^3/(3\pi^2)$. Global charge neutrality is then achieved by adjusting μ_e. The above processes are repeated many times until we get convergence.

[1] D. Page, J. M. Lattimer, M. Prakash, and A. W. Steiner, Astrophys. J. Suppl. Ser. **155**, 623 (2004).
[2] P. Haensel, A. Y. Pothekhin, and D. G. Yakovlev, *Neutron Stars 1* (Springer, New York, 2007).
[3] T. Takatsuka and R. Tamagaki, Prog. Theor. Phys. Suppl. **112**, 107 (1993).
[4] G. Baym and E. Flowers, Nucl. Phys. A **222**, 29 (1974).
[5] T. Takatsuka and R. Tamagaki, Nucl. Phys. A **478**, 785c (1988).
[6] E. E. Kolomeitsev and D. N. Voskresensky, Nucl. Phys. A **759**, 373 (2005).
[7] R. Knorren, M. Prakash, and P. J. Ellis, Phys. Rev. C **52**, 3470 (1995).
[8] N. K. Glendenning, Phys. Lett. B **114**, 392 (1982).
[9] N. K. Glendenning and S. A. Moszkowski, Phys. Rev. Lett. **67**, 2414 (1991).
[10] C. Ishizuka, A. Ohnishi, K. Tsubakihara, K. Sumiyoshi, and S. Yamada, J. Phys. G **35**, 085201 (2008).
[11] K. Tsubakihara, H. Maekawa, H. Matsumiya, and A. Ohnishi, Phys. Rev. C **81**, 065206 (2010).
[12] N. K. Glendenning and S. Pei, Phys. Rev. C **52**, 2250 (1995).
[13] G. F. Burgio, M. Baldo, P. K. Sahu, and H.-J. Schulze, Phys. Rev. C **66**, 025802 (2002).
[14] D. G. Ravenhall, C. J. Pethick, and J. R. Wilson, Phys. Rev. Lett. **50**, 2066 (1983).
[15] T. Tatsumi, M. Yasutake, and T. Maruyama, *Neutron Stars: The Aspect of High Density Matter, Equations of State and Observables*, edited by H. Uechi, S. T. Uechi, and B. D. Serot (Nova Science, Hauppauge, NY, 2012), Chap. 9.
[16] M. Hempel, V. Dexheimer, S. Schramm, and I. Iosilevskiy, arXiv:1302.2835.
[17] T. Maruyama, S. Chiba, H.-J. Schulze, and T. Tatsumi, Phys. Rev. D **76**, 123015 (2007).
[18] N. Yasutake, T. Maruyama, and T. Tatsumi, Phys. Rev. D **80**, 123009 (2009).

[19] M. Hashimoto, H. Seki, and M. Yamada, Prog. Theor. Phys. **71**, 320 (1984).
[20] Y. Mochizuki and T. Izuyama, Astrophys. J. **440**, 263 (1995).
[21] T. E. Strohmayer and A. L. Watts, Astrophys. J. **653**, 593 (2006).
[22] A. L. Watts, Annu. Rev. Astron. Astrophys. **50**, 609 (2012).
[23] H. Sotani, Mon. Not. Roy. Astron. Soc. **417**, L70 (2011).
[24] S. Ogata and S. Ichimaru, Phys. Rev. A **42**, 4867 (1990).
[25] N. Chamel, Phys. Rev. C **85**, 035801 (2012).
[26] C. J. Horowitz and K. Kadau, Phys. Rev. Lett. **102**, 191102 (2009).
[27] C. J. Horowitz, Phys. Rev. D **81**, 103001 (2010).
[28] G. Baym, H. A. Bethe, and C. J. Pethick, Nucl. Phys. A **175**, 221 (1971).
[29] R. D. Williams and S. E. Koonin, Nucl. Phys. A **435**, 844 (1985).
[30] W. G. Newton and J. R. Stone, Phys. Rev. C **79**, 055801 (2009).
[31] M. Okamoto, T. Maruyama, K. Yabana, and T. Tatsumi, Phys. Lett. B **713**, 284 (2012).
[32] H. Müller and B. D. Serot, Phys. Rev. C **52**, 2072 (1995).
[33] S. S. Avancini, D. P. Menezes, M. D. Alloy, J. R. Marinelli, M. M. W. Moraes, and C. Providencia, Phys. Rev. C **78**, 015802 (2008).
[34] K. Oyamatsu, M. Hashimoto, and M. Yamada, Prog. Theor. Phys. **72**, 373 (1984).
[35] K. Nakazato, K. Oyamatsu, and S. Yamada, Phys. Rev. Lett. **103**, 132501 (2009).
[36] M. Matsuzaki, Prog. Theor. Phys. **116**, 1 (2006).
[37] R. Ogasawara and K. Sato, Prog. Theor. Phys. **68**, 222 (1982).
[38] J. Boguta and A. R. Bodmer, Nucl. Phys. A **292**, 413 (1977).
[39] T. Maruyama, T. Tatsumi, D. N. Voskresensky, T. Tanigawa, and S. Chiba, Phys. Rev. C **72**, 015802 (2005).
[40] Y. Iwata, arXiv:1107.0464.
[41] B. Schuetrumpf, M. A. Klatt, K. Iida, J. A. Maruhn, K. Mecke, and P. G. Reinhard, arXiv:1210.8334.
[42] G. Watanabe, H. Sonoda, T. Maruyama, K. Sato, K. Yasuoka, and T. Ebisuzaki, Phys. Rev. Lett. **103**, 121101 (2009).
[43] G. Watanabe, K. Sato, K. Yasuoka, and T. Ebisuzaki, Phys. Rev. C **68**, 035806 (2003).
[44] T. Maruyama, K. Niita, K. Oyamatsu, T. Maruyama, S. Chiba, and A. Iwamoto, Phys. Rev. C **57**, 655 (1998).
[45] K. Oyamatsu and K. Iida, Phys. Rev. C **75**, 015801 (2007).
[46] J. W. Negel and D. Vautherin, Nucl. Phys. A **207**, 298 (1973).
[47] M. A. Preston and R. Bhaduri, *Structure of the Nucleus* (Addison-Wesley, Reading, MA, 1975).